The influence of wing–wake interactions on the production of aerodynamic forces in flapping flight

James M. Birch* and Michael H. Dickinson[†]

Department of Integrative Biology, University of California, Berkeley, CA 94720, USA

*Author for correspondence (e-mail: birchj@socrates.berkeley.edu)

[†]Present address: California Institute of Technology, mail code 138-78, Pasadena, CA 91125, USA

Summary

We used two-dimensional digital particle image velocimetry (DPIV) to visualize flow patterns around the flapping wing of a dynamically scaled robot for a series of reciprocating strokes starting from rest. The base of the wing was equipped with strain gauges so that the pattern of fluid motion could be directly compared with the time history of force production. The results show that the development and shedding of vortices throughout each stroke are highly stereotyped and influence force generation in subsequent strokes. When a wing starts from rest, it generates a transient force as the leading edge vortex (LEV) grows. This early peak, previously attributed to added-mass acceleration, is not amenable to quasi-steady models but corresponds well to calculations based on the time derivative of the first moment of vorticity within a sectional slice of fluid. Forces decay to a stable level as the LEV reaches a constant size and remains attached throughout most of the stroke. The LEV grows as the wing supinates prior to stroke reversal, accompanied by an increase in total force. At stroke reversal, both the LEV and a rotational starting vortex (RSV) are shed into the wake, forming a counter-rotating pair that directs a jet of fluid towards the underside of the wing at the start of the next stroke. We isolated the aerodynamic influence of the wake by subtracting forces and flow fields generated in the first stroke, when the wake is just developing, from those produced during the fourth stroke, when the pattern of both the forces and wake dynamics has reached a limit cycle. This technique identified two effects of the wake on force production by the wing: an early augmentation followed by a small attenuation. The later decrease in force is consistent with the influence of a decreased aerodynamic angle of attack on translational forces caused by downwash within the wake and is well explained by a quasi-steady model. The early effect of the wake is not well approximated by a quasi-steady model, even when the magnitude and orientation of the instantaneous velocity field are taken into account. Thus, the wake capture force represents a truly unsteady phenomenon dependent on temporal changes in the distribution and magnitude of vorticity during stroke reversal.

Key words: insect flight, flapping flight, wake structure, insect aerodynamics, DPIV, digital particle image velocimetry, flow visualization.

Introduction

Constructing an aerodynamic explanation for the forces generated during the flapping flight of insects is an important challenge in the study of both animal locomotion and fluid mechanics. Two complimentary experimental approaches have been used to study animal aerodynamics; one that focuses directly on the forces generated by flapping wings and another that attempts to reconstruct these forces by careful analysis of the resulting wake (Brodsky, 1994; Ellington, 1984; Rayner, 1979; Spedding et al., 1984). Due to their small size and rapid stroke frequency, direct measurement of forces on insect wings has not been possible. Although researchers have succeeded in capturing whole-body forces on tethered insects, such measurements are difficult to interpret because of contamination by wing mass inertial forces (Cloupeau et al., 1979; Dickinson and Götz, 1996; Wilkin and Williams, 1993;

Zanker and Götz, 1990). Although several studies have documented the flow pattern around the flapping wings of tethered insects (Brodsky, 1994; Dickinson and Götz, 1996; Ellington et al., 1996; Grodnitsky and Morozov, 1993; Willmott et al., 1997), these studies have not yet yielded quantitative measures of sufficient spatial and temporal resolution to permit estimates of either mean or instantaneous flight force. Even if fluid motion could be quantified to sufficient resolution, the reciprocating stroke pattern seen in insects still creates complex time-dependent flows that are difficult to quantitatively interpret.

Currently, two approaches attempt to circumvent these difficulties in measuring force production in living insects. The first is through the use of dynamically scaled robots programmed with kinematics derived from studies of flying or

tethered animals (Bennett, 1970; Dickinson et al., 1999; Ellington et al., 1996). A second approach is to computationally simulate a solution to the Navier–Stokes equation for the given pattern of motion and geometry (Hamdani and Sun, 2000; Liu et al., 1996, 1998). Such methods offer a complete solution for forces and flows in space and time but require extensive computing power and may be sensitive to model parameters.

Using dynamically scaled robots, recent studies suggest that the aerodynamic forces generated by the back-and-forth wing motion of hovering insects may be conveniently separated into four components due to: added-mass acceleration, translational circulation, rotational circulation and wake capture (Dickinson et al., 1999; Sane and Dickinson, 2002). The forces due to translational and rotational circulation are well-approximated by quasi-steady models (Sane and Dickinson, 2002). Thus, the time history of these force components is explained in large part by the temporal changes in wing kinematics and not the intrinsic time dependencies in the underlying flows. Furthermore, regardless of whether the kinematic motion generating vorticity is a steady propeller-like revolving motion around the wing hinge (translation) or the combination of this motion with a constant change in angle of attack (translation plus rotation), aerodynamic forces are generated by the prolonged attachment of a leading edge vortex. The physical bases of the forces generated during stroke reversal are less clear due to complications caused by the requisite change of wing motion. First, as the wing starts and stops at the beginning and end of each stroke it is subject to acceleration-reaction forces. These forces represent the impulsive change in momentum within the fluid imparted by the accelerating wing (Daniel, 1984) and are typically modeled in quasi-steady terms using a time-invariant added-mass coefficient (Sarpkaya, 1996). Because in such models the wing's influence on the surrounding fluid is mathematically equivalent to a time-invariant increase in wing mass, the 'added-mass' force tracks the time history of wing acceleration. However, results from experiments with impulsively and non-impulsively started bluff bodies show that peak transient forces are delayed with respect to wing acceleration, and thus quasi-steady models of acceleration-reaction forces are overly simplistic (Hamdani and Sun, 2000; Odar and Hamilton, 1964; Sarpkaya, 1982, 1991, 1992).

The second way in which the reciprocating stroke pattern complicates force generation is through the influence of the pre-existing wake. During stroke reversal, the wing sheds the vorticity generated during the prior stroke, and, as it reverses direction, the wing passes through this shed vorticity field. Under certain circumstances, this flow field can influence force at the start of the stroke, a mechanism previously termed 'wake capture' (Dickinson et al., 1999; Sane and Dickinson, 2001). Due to the complexity of the flows at stroke reversal, it is unlikely that wake capture will be amenable to quasi-steady approximations. Nevertheless, there are several means by which this wing–wake interaction might be incorporated within the current quasi-steady framework. First, the forces due to the influence of the wake might simply represent an augmentation of circulatory forces generated by the altered flow field at stroke reversal, a hypothesis analogous to the influence of gust on steady flight in aeroplanes (McCormick, 1995). This idea could be tested by directly measuring the actual velocity and orientation of the flow around the wing at the start of the stroke. Such 'corrected' values for instantaneous velocity and angle of attack could then be fed into a quasi-steady model for translational and rotational forces, and the results compared with measured values. In addition, if wake capture is simply an augmentation of steady-state circulatory forces acting throughout the stroke, the strength of the leading edge vortex should track the magnitude of the instantaneous force.

Another explanation for wake capture is that it represents an acceleration-reaction force caused by the rush of fluid against the wing at the start of each stroke. This effect is responsible for large drag forces on plants and sedentary animals in wave-swept environments (Daniel, 1984; Denny, 1988). Prior studies of wake capture demonstrated that a stationary wing, stopped after completing one stroke, continues to generate force as it is impacted by a jet of fluid within the wake (Dickinson et al., 1999). Simulations of this effect in two dimensions using computational fluid dynamics (CFD; Hamdani and Sun, 2000) are consistent with experimental results using identical kinematics (Dickinson, 1994). Because the wing is moving through a vortex jet, the acceleration-reaction forces should be greater than those expected if the wing were to accelerate through still fluid. This hypothesis could best be tested by careful quantification of flow structure combined with instantaneous force measurement. However, such an analysis would be hindered by the lack of a sufficiently accurate model of acceleration-reaction forces.

The difficulty encountered in constructing a reliable estimate of acceleration-reaction forces underscores a general problem with the multi-component quasi-steady approach. Although the net aerodynamic force may, for utility and convenience, be divided into components resulting from translational circulation, rotational circulation, added mass, etc., such divisions are to some extent arbitrary. All fluid forces acting on a submerged body result from physical interactions succinctly expressed in the Navier–Stokes equation. Although the utility of simpler time-invariant models is obvious for applications in both biology and engineering, such methods may not provide sufficiently accurate descriptions. Furthermore, as illustrated by the concept of 'added mass', such methods may obscure the underlying physical basis of observed forces. As discussed by Wu (1981), an equation that conveniently captures all aerodynamic force ($\mathbf{F}$) acting on a solid body within a fluid is:

$$\mathbf{F} = -\rho \, \frac{d\boldsymbol{\gamma}}{dt} + m' \, \frac{d\mathbf{U}}{dt} \,, \tag{1}$$

where ρ is fluid density, t is time, m' is the mass of the fluid displaced by the solid body, and $\mathbf{U}$ is the velocity of the body.

The term **γ** represents the first moment of vorticity (**ω**), defined as:

$$\boldsymbol{\gamma} = \int_{R_\infty} \mathbf{r} \times \boldsymbol{\omega} \mathrm{d}R \,, \qquad (2)$$

where **r** is the position vector, **ω** is the vorticity and d*R* is the element of area. The second term in equation 1 represents the force generated as the volume of an accelerating body displaces fluid and, in biological models, is often incorporated as one of two components of the acceleration-reaction force (the second component of the acceleration-reaction force takes into account the change in fluid momentum caused by the accelerating body, which is distinct from the fluid displaced by the body's volume; see Denny, 1993). For sufficiently thin plates, the contribution of the second term in equation 1 is negligible. All components of the current quasi-steady model of flapping flight (translation, rotation, wake capture and the volume-independent component of acceleration reaction) are embodied within the first term of equation 1. Thus, according to this unified equation, forces on the body result from time-dependent changes in both the magnitude and the distribution of vorticity. For example, in the case of a wing moving with constant bound vorticity, the vector **r** is the only time-dependent variable, which increases as the wing moves away from the shed starting vortex. Under these conditions, equation 1 reduces to the Kutta–Joukowski equation (see Wu, 1981). Under more complicated conditions, such as during an impulsive start or stroke reversals of a flapping wing, the growth and decay of vorticity at fixed locations within the flow field will also contribute to force production, as will the shedding of vortices. Equation 1 is more useful in an experimental context than the Navier–Stokes equation, because forces may be calculated without knowledge of the pressure distribution (Noca et al., 1999), which is not directly measurable using such methods as digital particle image velocimetry (DPIV).

In this study, we use DPIV (Raffel et al., 1998) to quantify chord-wise flow dynamics during the flapping motion of a robotic wing. The DPIV is paired with simultaneous force measurement, permitting a direct comparison of flow dynamics and force production. Our basic approach is to examine the pattern of fluid flow and force generation during a continuous sequence of strokes starting from rest. Of particular interest is the comparison of the initial stroke, when the wing begins moving through still fluid, with later strokes, when the wing must move through the shed vorticity of prior strokes. The results show that large force peaks, previously attributed to added mass, are best explained *via* the vortex moment equation as a rapid growth in vorticity and not by any quasi-steady formulation in which forces are proportional to the instantaneous magnitude of vorticity. Furthermore, they show that the influence of the wake on force generation may be divided into two phases during each stroke: an early augmentation (wake capture), followed by a subsequent attenuation. Like the initial force peak generated by a wing starting from rest, wake capture cannot be explained by the instantaneous magnitude of vorticity. Rather, the wake capture forces are best explained by the altered growth rate of vorticity as the wing passes through the shed vorticity of the prior stroke. The later decrease in force results from an attenuation of translational circulation caused by downwash induced by the wake. Collectively, these findings provide a direct view of wake dynamics during flapping flight and quantify the potential influence of the shed vorticity of previous strokes on force production. They also provide empirical results with which to test recent numerical simulations based on nearly identical stroke kinematics (Ramamurti and Sandberg, 2002; Sun and Tang, 2002).

Materials and methods

The dynamically scaled robotic fly used in this study has been described in detail elsewhere (Dickinson et al., 1999; Sane and Dickinson, 2001) and will only be briefly summarized here. The robot consists of six stepper motors and two coaxial arms immersed in a tank of mineral oil (Fig. 1A). A sensor at the base of one wing measures parallel and perpendicular forces from which we calculate total force or separate lift, drag and radial force components. The wing was fabricated from a 2.25 mm acrylic sheet, cut in the shape of a *Drosophila* wing with a total length of 0.25 m when attached to the force sensor. Force data were collected at 100 Hz using a National Instruments data acquisition board (BNC 2090) and filtered off-line using a zero phase delay low-pass digital Butterworth filter with a cut-off frequency of 10 Hz, roughly 60 times the wing stroke frequency. The wing and arm apparatus were place in a 1 m×1 m×2 m Plexiglas tank filled with 1.8 m³ of mineral oil with a density of 0.88×10^3 kg m⁻³ and a kinematic viscosity of 1.2×10^{-4} m² s⁻¹. We used a custom program written in MATLAB to generate arbitrary kinematic patterns and to record and analyze data.

These experiments focused on simultaneous measurement of instantaneous forces and flows using a simple back-and-forth wingbeat pattern. This pattern was chosen because all four mechanisms of force production possible in flapping flight are present (Sane and Dickinson, 2001). The wing flapped through 160° of amplitude with a 45° angle of attack at midstroke. Following the convention of Sane and Dickinson (2001), we defined rotation parameters (τ) as percentages of a complete wing stroke. Thus, τ_0 represents the time when wing rotation begins, τ_f represents flip timing (when the midpoint of the flip occurs) and $\Delta\tau$ is flip duration. In this experiment, $\tau_0 = -0.12$, $\tau_f = -0.06$ and $\Delta\tau = 0.12$. Thus, wing rotation was advanced relative to stroke reversal by 12% of the stroke period and was completed at stroke reversal. The wings did not deviate from the stroke plane, and the upstroke and downstroke were identical by mirror symmetry. However, slippage between the teeth of the gear box introduced inaccuracies of approximately 1–5° in the angle of attack, which could result in small differences between up- and downstrokes. Flapping the wing at 168 mHz generated maximum tip velocities at midstroke of 0.31 m s⁻¹, with a mean wingtip velocity over the entire stroke
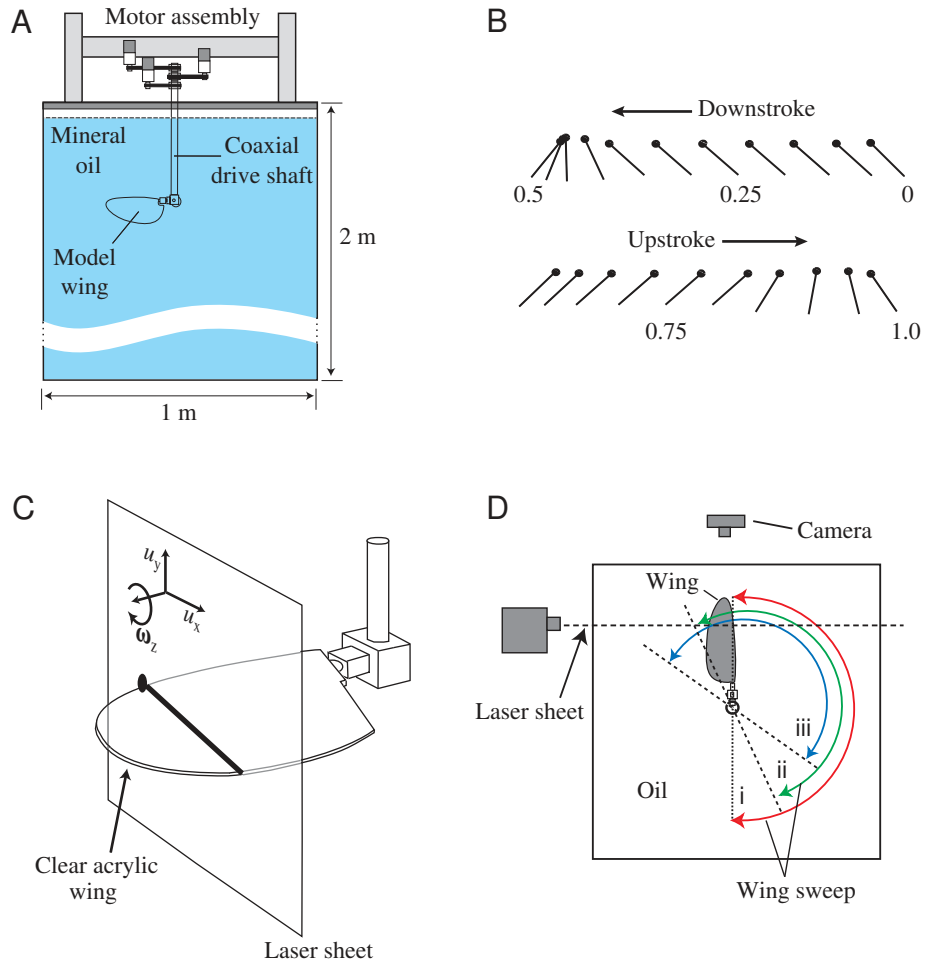
Fig. 1. Experimental apparatus and procedure. (A) Each arm of the robotic insect consists of a flapping wing controlled by three stepper motors. (B) Wing position arranged as two-dimensional projections. The line represents the wing chord, with the circle indicating the leading edge. Numbers indicate the value of $\hat{t}$. (C) Mini-YAG lasers create a 2.5 mm-thick sheet of light at 0.65R. By seeding the oil with small air bubbles and calculating their movement between two laser flashes separated by a 2 ms delay, we captured fluid velocity (u) in the x and y direction and subsequently calculated z vorticity (ω). (D) To collect time series data, we timed the firing of the laser and the starting position of the wing so that the wing was in front of the camera at the desired phase of the stroke (i). After collecting an image at that position, the laser delay was increased by 100 ms, and the starting position of the wing was set backwards so that the wing passed in front of the camera and the flow was illuminated at a later point in the stroke cycle (ii). This laser timing/wing positioning adjustment was repeated to reconstruct a complete series of flow visualizations.

of 0.26 m s^{-1}. These kinematics corresponded to a Reynolds number of approximately 160 based on the velocity of the chord section in which we visualized flow. In order to correlate force and flow information, we express time during the stroke as a non-dimensional parameter, $\hat{t}$, such that $\hat{t}=0$ at the start of the downstroke, and $\hat{t}=1$ at the end of the subsequent upstroke (Fig. 1B).

Flow visualization

We used digital particle image velocimetry (DPIV) to quantify the flow structure in a slice of fluid centered on the wing. Prior to each experiment, we seeded the oil with air forced through a ceramic water filter stone to create a dense bubble field. After larger bubbles rose to the surface, the remaining bubbles, although slightly positively buoyant, did not rise perceptibly during capture of the paired DPIV images. Forces measured with bubbles in the tank were identical to those measured in the absence of bubbles, indicating that their introduction did not alter the basic properties of the medium. A commercial software package controlling a dual Nd-YAG laser system (Insight v. 3.2, TSI Inc., St Paul, MN, USA) created two identically positioned light sheets approximately 2.5 mm thick separated by 2 ms (Fig. 1C). These light sheets were positioned at 0.65R (R=length of one wing) and timed to

fire when the wing chord was directly in front of a high-speed video camera placed perpendicular to the laser sheet (Fig. 1D). We chose 0.65R as our point of measurement because, in a prior DPIV study, this was the position at which the leading edge vortex was still attached and exhibited near-maximal spanwise vorticity (Birch and Dickinson, 2001). After saving the captured images from the two laser flashes, the trigger for the laser was advanced 100 ms, and the starting position of the wing moved backwards so that at the start of the next sequence it would pass in front of the camera at a slightly later point in the sequence of stroke cycles. In this way, we captured the fluid flow around the wing through four downstroke/upstroke cycles at 100 ms intervals. In order to facilitate a more intuitive interpretation of fluid motion, we subtracted wing speed from fluid velocity, so that the fluid is visualized from a frame of reference that follows the span of the wing (Fig. 2).

For each image-pair captured, a cross-correlation of pixel intensity peaks with 50% overlap of 64 pixel×64 pixel interrogation areas yielded a 30×30 array of vectors. The effectiveness of our bubble-seeding density was evident during vector validation. After creating velocity vectors for 236 images (59 images stroke^{-1} × four strokes), the magnitude of only two out of a possible 212 400 vectors was greater than three standard deviations of the mean length in their respective
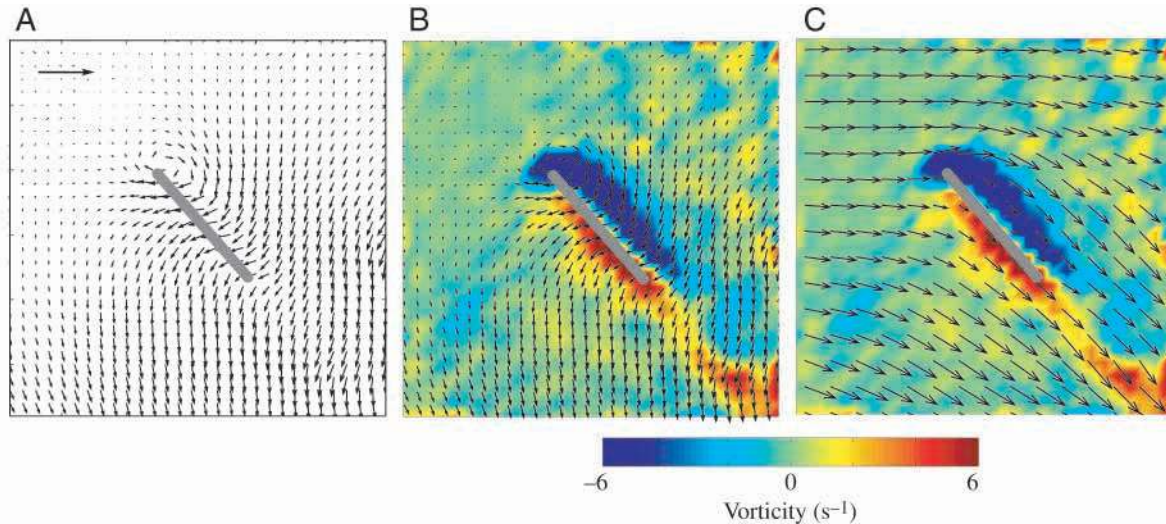
Fig. 2. Convention for displaying fluid velocity. (A) From the wing's frame of reference, the wing (gray bar) is moving to the left, with instantaneous fluid motion indicated by the arrows. The length of the calibration arrow represents 0.40 m s^{-1} in all panels. Field of view is approximately 0.28 m×0.28 m. (B) The identical velocity plot with vorticity added in pseudocolor. Blue represents clockwise vorticity, red represents counter-clockwise vorticity. (C) Fluid motion with wing speed subtracted and only every other vector plotted. This convention will be used throughout the paper.

images. These two deleted values were filled by interpolation of a mean value from a 3×3 nearest-neighbor matrix. Aside from these two corrections, we performed no additional filtering or modification of the flow data.

A program written in MATLAB was used to calculate vorticity from the velocity fields and perform all subsequent flow measurements. By gathering a complete time history of fluid velocity through four strokes, we could observe the growth of vorticity in select regions around the wing throughout each stroke and compare velocity and vorticity between strokes. In some calculations, vorticity panels were subject to a threshold mask that recognized only the top 10% of vorticity values. This criterion was applied to all panels of all strokes and resulted in the description and quantification of four major regions of vorticity: the leading edge vortex (LEV), the under wing shear layer (USL), the translational starting vortex (TSV) and the rotational starting vortex (RSV). To isolate and visualize the wake created by prior strokes from the flows generated during a current stroke, we subtracted the instantaneous velocity fields measured during the first stroke from those measured during the fourth stroke. These resulting differences in both flow and forces represented the influence of vorticity shed during prior strokes on subsequent aerodynamic performance.

In order to estimate sectional forces from the DPIV images, we calculated the first moment of the vorticity field, γ, using the center of the wing as the origin for the position vector. A custom program in MATLAB then calculated the time derivative of this term. Multiplying by –1 and fluid density provides the instantaneous sectional force predictions to compare with measured forces.

Estimating the aerodynamic angle of attack

To test whether a corrected quasi-steady model can explain

the influence of the wake, it is necessary to estimate the distortion of the aerodynamic angle of attack, α_{aero}, caused by shed vorticity. Although the concept of α_{aero} is straightforward, in practice its measurement is problematic. Because the wing functions as an impermeable boundary, fluid upstream is deflected gradually downward from the free stream orientation until it flows parallel to the wing's surface. This deflection is not due to the presence of chord-wise vorticity and is present even in two-dimensional flow. In three-dimensional flow, the presence of chord-wise vorticity from the wing tip or other sources deflects the flow downward to an even greater degree than in the two-dimensional case. Thus, any experimental measurement of downwash should be made relative to the deflection required by the boundary condition of tangential flow at the surface of the wing. In the case of the model fly wing, the downwash caused by the wake of past strokes may be conveniently measured by comparing flows of a starting stroke, when the wake is just developing, with later strokes, when the wake is fully entrained. Another complication in measuring α_{aero} is that the effect of fluid incidence on circulatory forces is not restricted to any specific region ahead of the wing. Thus, it may be misleading to measure the effect of downwash within a defined interrogation region. We chose a region upstream of the wing that was large enough so that both the mean α_{aero} and fluid velocity during a starting stroke were similar to values dictated by wing kinematics.

Results

Time course of forces and flows

The time history of forces during flapping was similar to that described elsewhere (Dickinson et al., 1999; Sane and Dickinson, 2001). In the first stroke, there was an initial peak
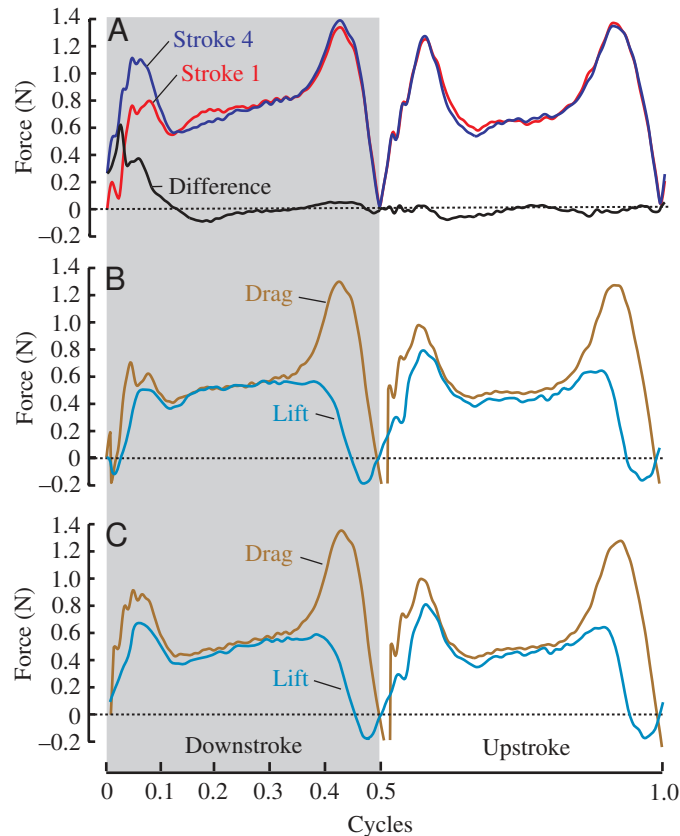
Fig. 3. Time history of aerodynamic forces during one complete stroke cycle. (A) Net force. The red line is the net force during the first stroke; the blue line is the force during the fourth stroke. The black line is the difference in net force between the fourth and first strokes. At the start of the downstroke, the fourth stroke generates considerably more force than the first stroke but generates less force as translation continues. Note that these differences nearly vanish during the upstroke of each stroke, since by the start of the first upstroke, the dynamics of the wake have reached a limit cycle. The gray box represents the downstroke and the time during which the digital particle image velocimetry (DPIV) images in Figs 4, 5, 9 and 10 were captured. (B) Lift and drag for stroke one. (C) Lift and drag for stroke four.

in force (to approximately 0.75–0.8 N) at the onset of translation followed by a sharp decline and then a slow rise (Fig. 3A,B). Prior to stroke reversal the force increased sharply again, due to the onset of wing rotation.

The forces generated in the fourth stroke (Fig. 3A,C) were similar to those generated during the first, with two distinct differences. First, the force peak at the onset of translation was larger than at the start of the first stroke. Second, following the decline of the initial force peak, total force in the fourth stroke drops below that of the first stroke, not reaching a similar level until approximately $\hat{t}$=0.3. After subtracting the total force of stroke one from that of stroke four, the difference can be divided into two phases; an initial phase in which the force during stroke four is higher than stroke one and a subsequent phase when the force during stroke four is less than in stroke

one (Fig. 3A, black trace). The first phase is indicative of wake capture, when the wing reverses direction and moves through the shed vorticity field of the previous stroke. The second phase, when the fourth stroke forces are lower, occurs after the leading edge vortex (LEV) has formed and translational circulation dominates total force production (Sane and Dickinson, 2001).

Plots of vorticity and velocity through the downstroke of the first and fourth strokes provide a quantitative comparison of flow dynamics. In the first stroke (Fig. 4), the initial force peak, which we attribute to acceleration-reaction force, occurs as the LEV grows (compare the red arrow and blue region, $\hat{t}$=0.03–0.07). The growth of the LEV occurs as a sheet of counter vorticity under the wing rolls up into a translational starting vortex (TSV). The LEV reaches its final size after approximately 1.5 chord lengths of travel. During subsequent translation in which the wing moves at constant velocity away from the TSV, the LEV reaches a stable size and force production remains relatively constant ($\hat{t}$=0.17–0.38). At $\hat{t}$=0.39, the wing begins to rotate, which increases both the size of the LEV and the magnitude of the net force. This increase in force is due to the contribution of rotational circulation and the influence of the increased angle of attack on translational circulation (Sane and Dickinson, 2002). As the wing rotates, the under wing shear layer (USL) rolls up into a vortex under the trailing edge. This vortex counterbalances the additional vorticity within the LEV that results from rotation and thus represents a rotational starting vortex (RSV). Force drops precipitously at stroke reversal when translational velocity falls to zero. Rotation results in the shedding of the LEV and RSV, which form a counter-rotating pair upstream of the wing at the onset of the next stroke.

At the beginning of the fourth stroke, fluid flow displays a more complicated pattern than in the first stroke due to the presence of shed vorticity within the wake (Fig. 5). As the wing travels into the vortex pair composed of the shed LEV and RSV, these two vortices direct a jet of high velocity fluid towards the underside of the wing ($\hat{t}$=0.00–0.09), resulting in an instantaneous force peak of 1.1 N at $\hat{t}$=0.05. As the wing continues translating, the vorticity from the remnants of the last LEV, combined with a new USL, eventually roll up into a new starting vortex, which is substantially larger than the starting vortex created during the first stroke (compare Fig. 4, $\hat{t}$=0.10 with Fig. 5, $\hat{t}$=0.10). The RSV lies directly beneath this new combined translational starting vortex, directing another jet of fluid rearward under the trailing edge. With continued motion, the wing passes through the wake (Fig. 5; $\hat{t}$=0.15) and forces drop to nearly half the peak level (Fig. 5; 0.56 N at $\hat{t}$=0.15).

An additional vortex structure seen from $\hat{t}$=0.00 to $\hat{t}$=0.19 in the fourth stroke (but absent during the same period in stroke one) results from the two-dimensional view of the complicated three-dimensional structure of the wake at stroke reversal. Two concentrations of clockwise vorticity (blue) are visible at the start of stroke four: the starting vortex from rotation described above and a slice through the arc-shaped tip vortex of the prior stroke (Fig. 6). Note that as the wing moves through the stroke, it
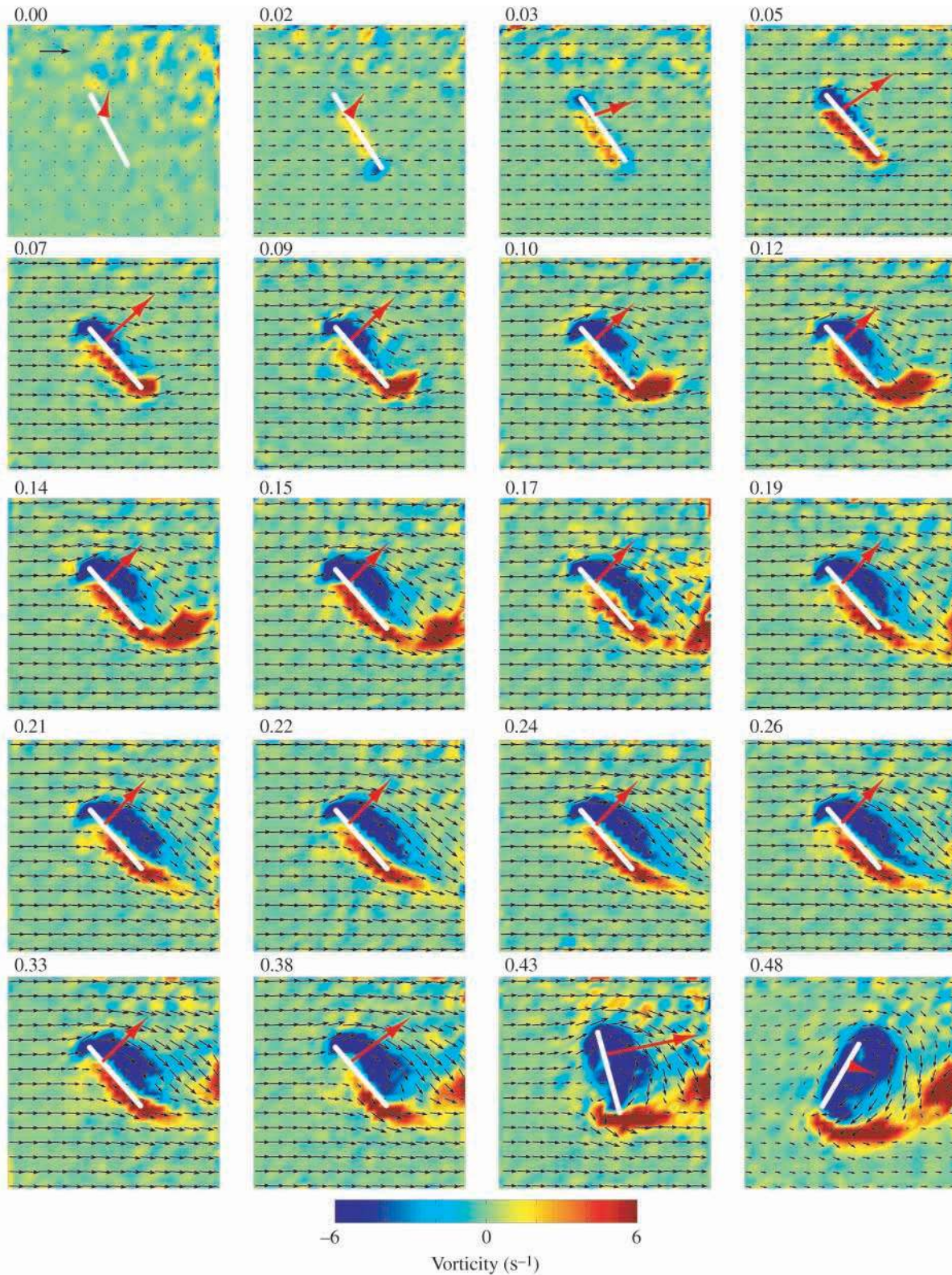
Fig. 4. Flow visualization and force generation during the first downstroke. The first 16 frames are 100 ms apart; numbers in the upper left-hand corners represent the value of $\hat{t}$. In this representation, fluid moves to the right over the wing (white bar) and, for clarity, velocity vectors are shown undersampled by a factor of 2. For scale, the length of the black calibration arrow in the first panel equals 0.40 m s^{-1}. Pseudocolor represents vorticity; length of the red arrows represents the instantaneous total force. Note the slow build-up of the leading edge vortex (blue region; $\hat{t}$=0.03–0.10) and the shedding of the starting vortex from the trailing edge (red region; $\hat{t}$=0.09–0.19). Near $\hat{t}$=0.40, the wing begins to slow for stroke reversal, rotates and sheds trailing edge vorticity (red region).
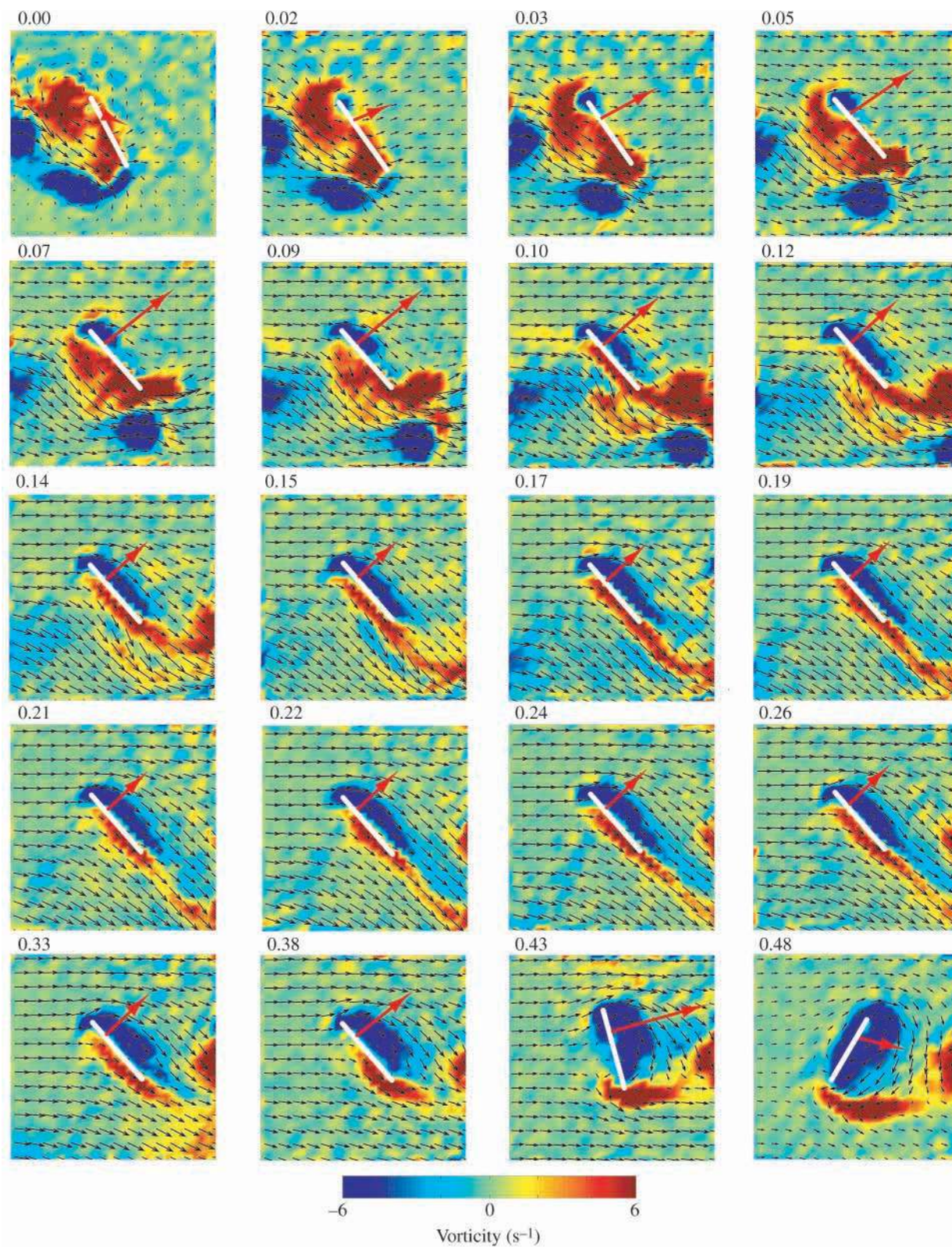
Fig. 5. Flow visualization and force generation during the downstroke of stroke four. Panels represent identical time points as in Fig. 4. Note the difference between this stroke and stroke one at frames $\hat{t}$=0.00–0.14 due to the wing traveling through the shed vorticity of the prior upstroke. Note also the concomitant increase in force (compare red arrow length at $\hat{t}$=0.05–0.10 between strokes one and four). Flow vector lengths are to the same scale as in Fig. 4.
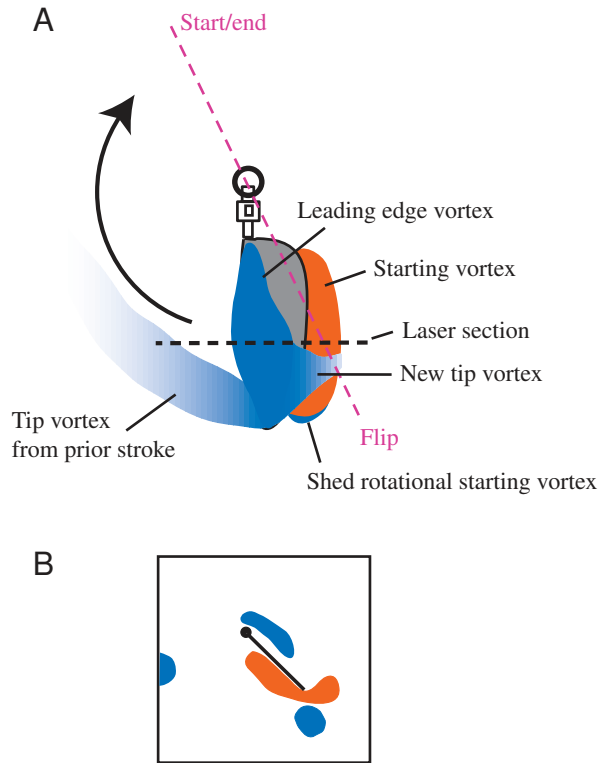
Fig. 6. Side views show tip vorticity just after stroke reversal. (A) As illustrated by this cartoon looking down on the wing from above, the tip vortex is curved and roughly follows the sweep of the wing tip. (B) Images captured at this time show two regions of clockwise vorticity (blue) beneath the wing: the shed rotational starting vortex and an oblique slice of the tip vortex.

eventually reaches fluid where the tip vortex has moved downward. By $\hat{t}=0.19$, the only remaining influence of the prior stroke's tip vorticity is the induced downward flow, which may be seen by comparing the flow pattern at $\hat{t}=0.19$ in Figs 4 and 5.

Fig. 7 provides a schematic summary representation of the growth and movement of the major areas of vorticity as the wing goes through one complete stroke cycle. At the start of the downstroke, the arrangement of vortices is relatively simple, consisting of a developing LEV, an attached TSV and a USL. As the stroke proceeds, the TSV sheds ($\hat{t}=0.20$). Near the end of the downstroke, the wing slows and rotates and an RSV develops at the trailing edge. After reversing direction, the wing slices through both the LEV and the RSV at the start of the upstroke. This movement through the previous vorticity accelerates slightly the build-up of the new LEV (LEV$_2$ at $\hat{t}=0.52$). Just after translation begins, a new USL forms (USL$_2$ at $\hat{t}=0.55$) that is connected to the shed TSV (TSV$_2$). This new starting vortex (TSV$_2$) is part of a doublet with the shed RSV from the prior stroke (RSV$_1$). This doublet is shed as the wing progresses through translation and, upon stroke reversal, the process begins again.

First moment of vorticity during an impulsive start

In order to measure flow near the wing with sufficient spatial resolution, we deliberately chose a field of view that did not capture all vorticity throughout repeating strokes. In addition, an enlarged planar view would be insufficient to measure the salient features of the three-dimensional flow structures generated by the flapping wing. For these reasons, it was not possible to estimate forces from the time-derivative of the first moment of vorticity (equation 1) throughout the entire stroke. However, the flow structure at the beginning of the first stroke was sufficiently compact to allow an estimate of forces based on equation 1. This calculation should provide insight into the physical basis of the force transient at the start of the first stroke. While the magnitude of the acceleration term in equation 1 contributed little to the overall force, the time course of the calculated sectional force based on the vortex moment matches well the measured lift and drag over the first 16% of the stroke (Fig. 8). After that, vorticity leaving the field of view renders the estimate inaccurate. If the predicted sectional lift is multiplied by wing length, the resulting peak is roughly 50% greater than that of the measured lift. Such a discrepancy is expected because we deliberately measured flow within the section where chord-wise vorticity has been shown to be greatest (Birch and Dickinson, 2001). The results, combined with an inspection of Fig. 4, suggest that the early force transient is due to the rapid growth of vorticity at the start of the stroke.

Influence of wake on force production

Unfortunately, it was not possible to calculate force from the first moment of vorticity during wake capture because the flow distribution extended well beyond our field of view (Fig. 5). Although methods exist to compensate for vorticity flux across the boundary of a control volume in two dimensions (Noca et al., 1997), these methods did not prove robust when applied to our data. However, because both strokes follow identical kinematics, subtracting flow fields of stroke one from those of stroke four provides an explicit picture of the wake from prior strokes, independent of the fluid motion created by wing motion within the stroke itself. Such reconstructions should provide insight into the physical basis of forces caused by the presence of the wake. Fig. 9 shows the reconstructed fluid velocity of the wake, representing the point-by-point difference in flow between the fourth and first stroke. From $\hat{t}=0.00$ to $\hat{t}=0.05$, the primary feature of the difference in flows between the fourth and first strokes is an area of elevated fluid velocity upstream of the wing. This barbell-shaped jet of fluid has two regions of peak velocity: an upper area corresponding to the flow between the counter-clockwise LEV and the clockwise remnant of the tip vortex from the prior stroke and a lower area representing the jet produced from the prior stroke between the counter-clockwise LEV and the clockwise RSV. This jet moves rearward, just under the trailing edge from $\hat{t}=0.02$ to $\hat{t}=0.12$. The panels also show an induced downward flow, which is strongest from $\hat{t}=0.09$ to $\hat{t}=0.15$ and then dissipates from $\hat{t}=0.22$ to $\hat{t}=0.33$ as the stroke proceeds. By stroke reversal ($\hat{t}=0.43–0.48$), the influence of the wake is barely measurable.
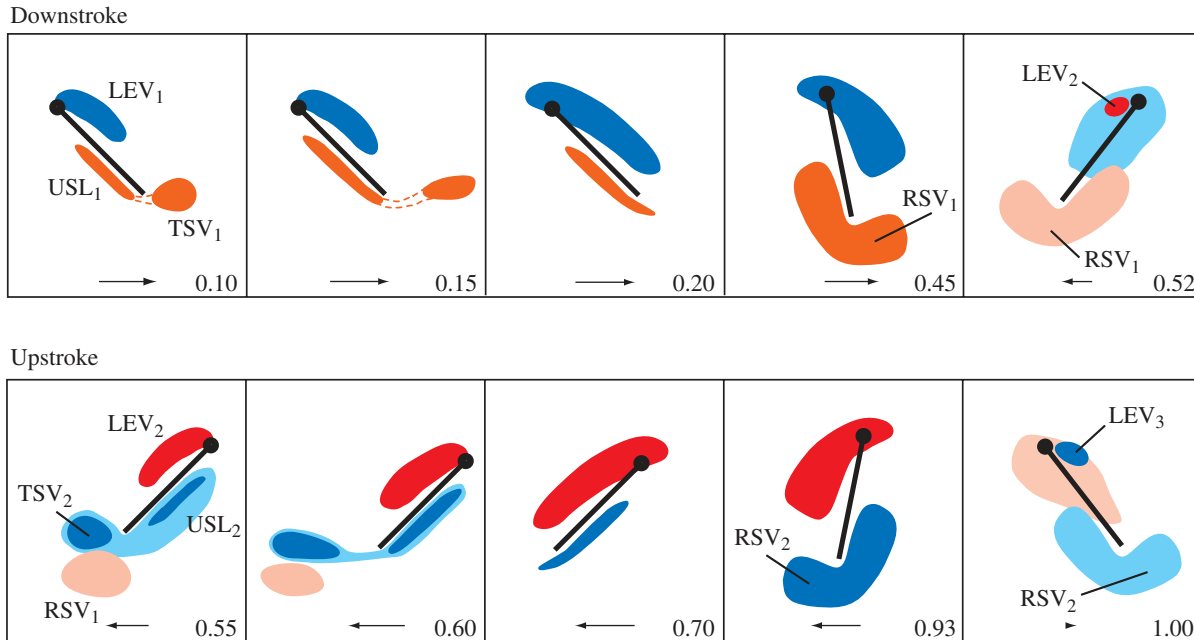
Downstroke

Upstroke

Fig. 7. Diagrammatic summary of wake dynamics. Each panel shows the growth and shedding of three vortices. Warm tones (reds) represent counter-clockwise vorticity; cool tones (blues) represent clockwise vorticity. Lighter shades represent vorticity that was generated in the previous stroke. Numbers in the bottom right-hand corners indicate the proportion of the stroke cycle completed. Arrow length is proportional to instantaneous fluid velocity. USL, underwing shear layer; LEV, leading edge vortex; TSV, translational starting vortex; RSV, rotational starting vortex.

The vorticity fields corresponding to the reconstructed velocity fields of Fig. 9 are shown in Fig. 10. From $\hat{t}=0.02$ to $\hat{t}=0.07$, there is a small region of clockwise vorticity (blue) at the leading edge, signifying that the LEV is slightly stronger at the start of stroke four compared with stroke one. The situation reverses, however, and by $\hat{t}=0.09$ a counter-clockwise vorticity (red) appears at the leading edge, indicating that the LEV of stroke four is weaker than in stroke

one. By $\hat{t}=0.12$, a clockwise layer of vorticity (blue) forms just above the surface of the wing, bounded above by a counter-clockwise layer (red). This indicates that from $\hat{t}=0.12$ to $\hat{t}=0.26$, the LEV in stroke four is more closely attached to the surface of the wing than in stroke one. After $\hat{t}=0.30$, the difference in the structure of the LEVs of the two strokes is quite small, consistent with the near identical force records at this phase in the cycle.

To test whether quasi-steady equations corrected for the values of the instantaneous velocity field might be capable of explaining either the early augmentation or late attenuation of forces during stroke four (Fig. 3A), we quantified the mean velocity and orientation of fluid within a $260\,\text{cm}^2$ region in front of the wing (Fig. 11A). Fluid velocity within this interrogation region, measured from $\hat{t}=0.00$ to $\hat{t}=0.20$, was approximately that of the robotic flapping speed during stroke one (Fig. 11B). In addition, the wing intercepts fluid during the first downstroke at an angle very close to the 45° kinematic angle of attack (Fig. 11C). Although the mean fluid velocity within this same region was 52% higher during the fourth
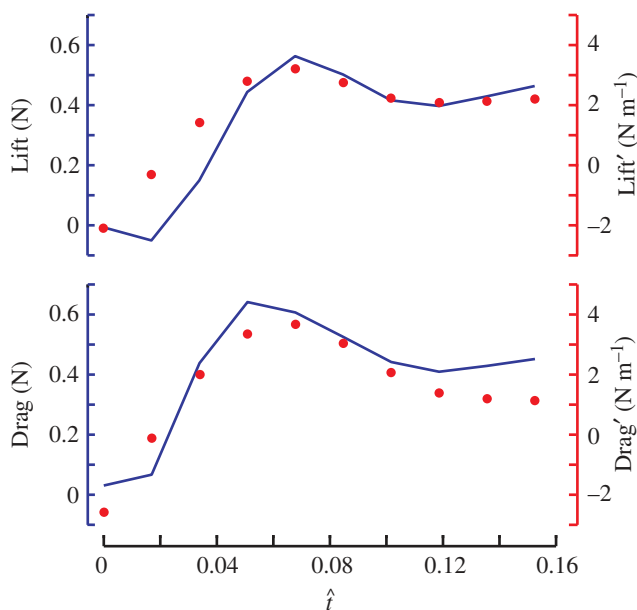

Fig. 8. Predictions of equation 1 and measured forces give similar time histories at the start of stroke one. The x-axis covers the first 16% of stroke one. Blue traces (left-hand y-axes) show measured lift and drag forces. Red circles (right-hand y-axes) plot values of sectional lift and drag calculated from the vortex moment calculation in equation 1. Predictions beyond $\hat{t}=0.15$ were unreliable because starting vorticity moves out of the visualized frame.
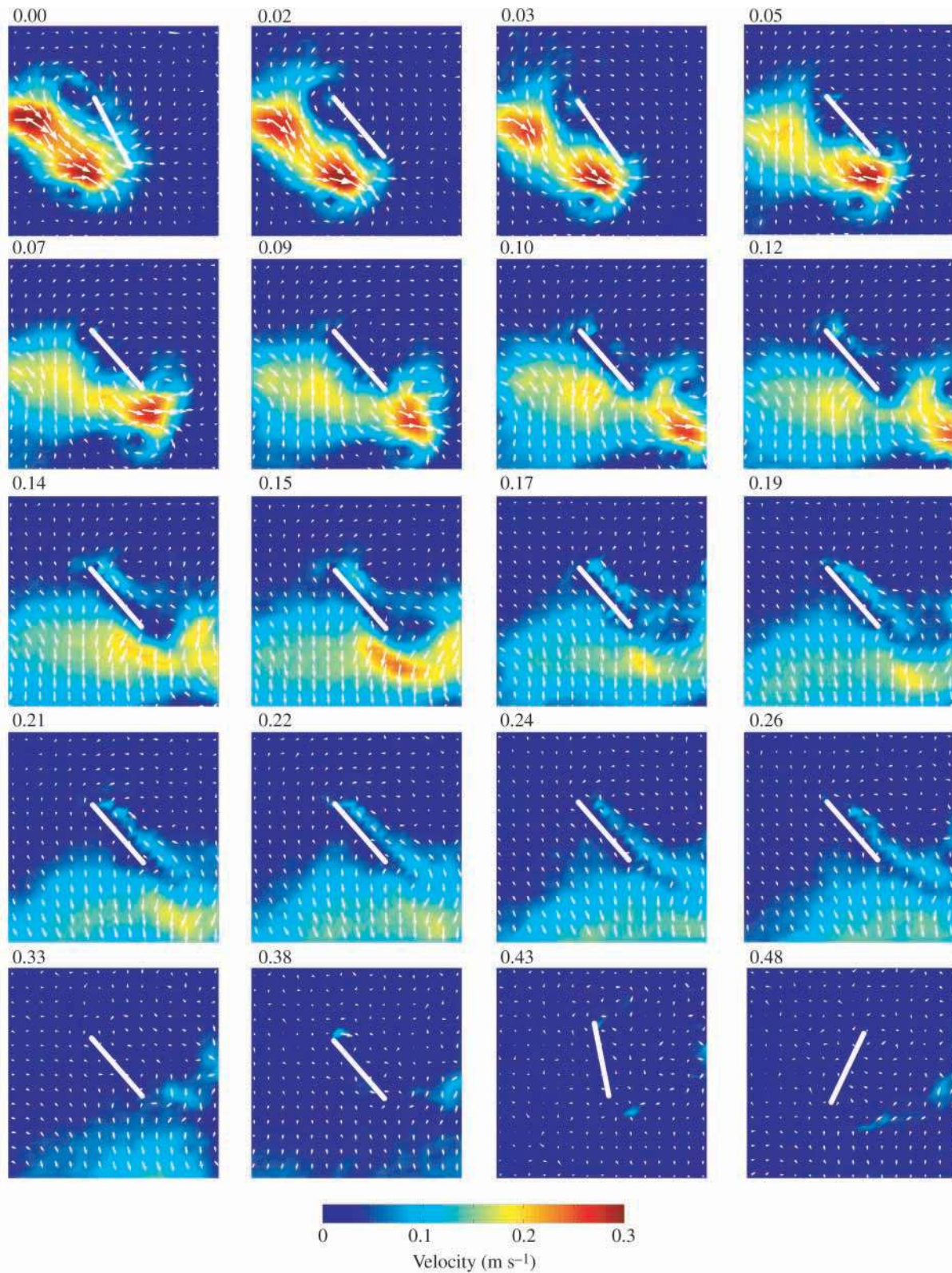
Fig. 9. Subtractive reconstruction of wake velocity fields. Pseudocolor represents the magnitude of the velocity difference between strokes four and one. Arrows indicate direction and magnitude of flow. Note the two regions of high fluid velocity from $\hat{t}$=0.00 to $\hat{t}$ 0.05, which represent the influence of the shed vorticity from the prior stroke. Also note the downward component of velocity in the flow vectors from $\hat{t}$=0.09 to $\hat{t}$ 0.33, indicating that through most of the stroke, stroke four encounters fluid at a lower aerodynamic angle of attack than during stroke one. After the stroke has completed 38% of a cycle ($\hat{t}$=0.38–0.48), there is no difference in fluid velocity between the first and fourth strokes. Flow vector lengths are to the same scale as in Fig. 4.
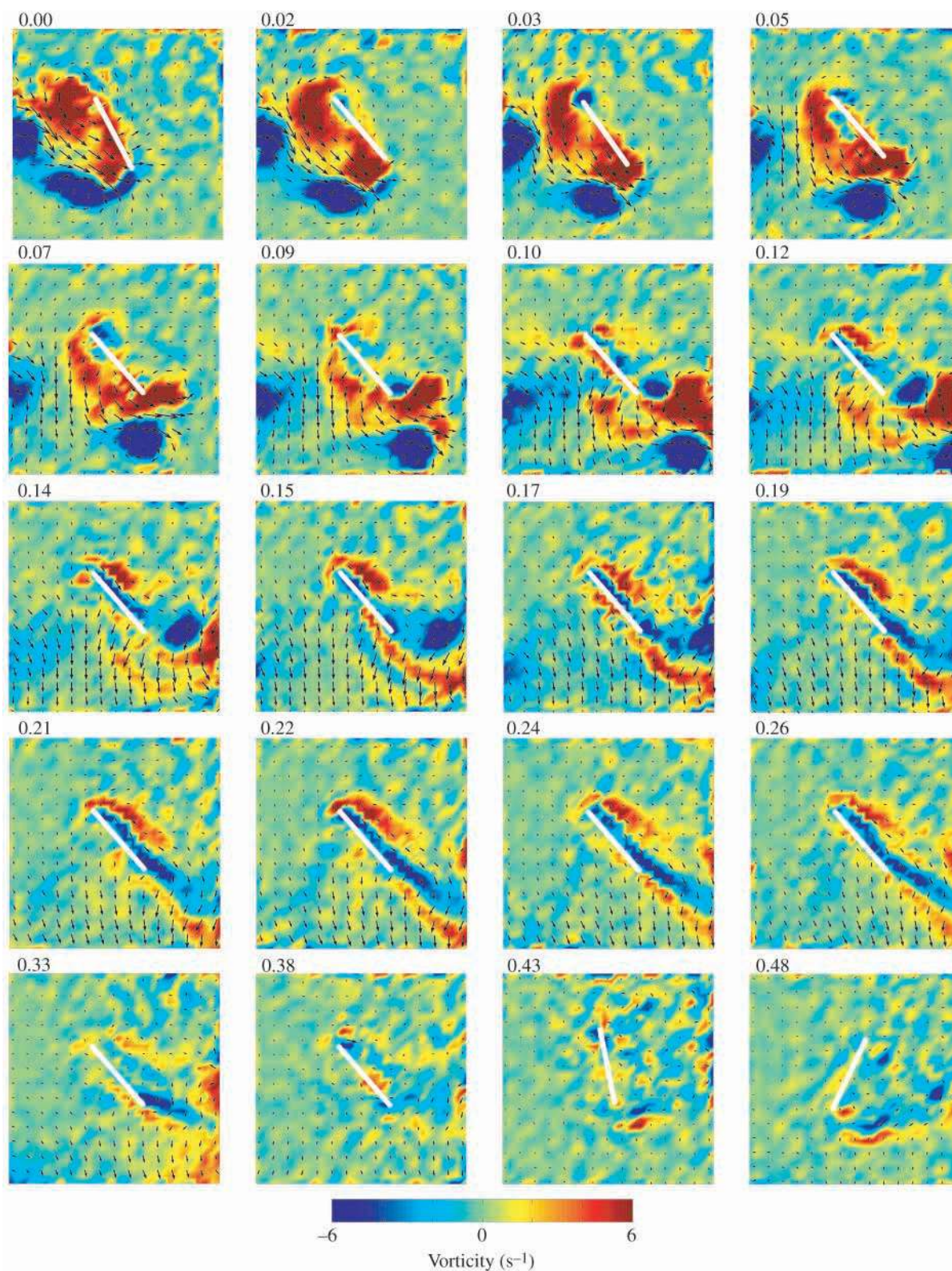
Fig. 10. Subtractive reconstruction of wake vorticity fields. Pseudocolor represents the magnitude of the difference in span-wise vorticity between strokes four and one. Arrows, representing velocity differences, are identical to those in Fig. 9. Note the greater amount of both clockwise and counter-clockwise vorticity early in the stroke (indicating greater vorticity during stroke four), and the diminution of any vorticity difference near the end of the stroke ($\hat{t}$=0.38–0.48.)
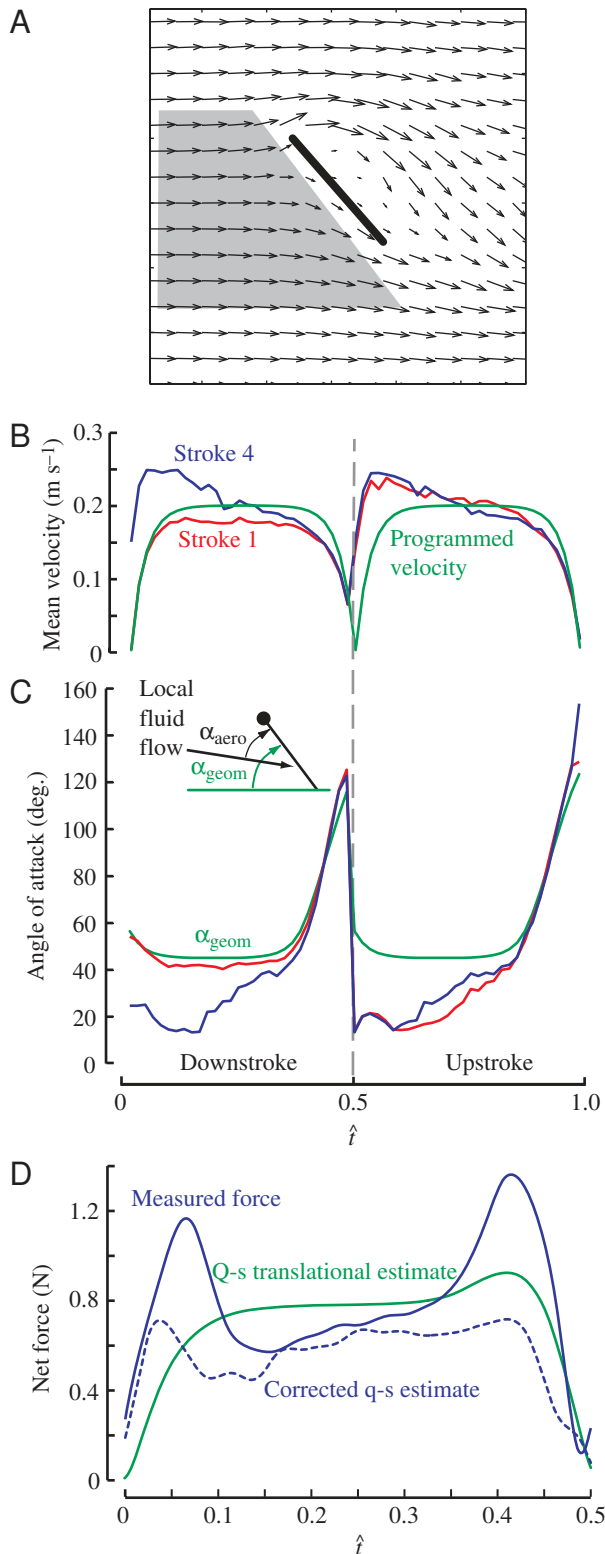
A

B

C

D

Fig. 11. The wake of prior strokes results in both an increase in fluid velocity and a reduction in the aerodynamic angle of attack (α_{aero}). (A) Representative panel with selected area from which we estimated the mean angle of attack and mean resultant velocity for both the first and fourth strokes. This region retained approximately the same area through wing rotation and flipped to the right side of the panel when the wing reversed direction. (B) Mean resultant velocity in the same region shows higher values during stroke four than stroke one. The green line shows fluid velocity predicted from wing kinematics. (C) Because of the downwash, α_{aero} is much less during the fourth stroke (blue) than the first (red). This difference nearly disappears during the upstroke when downwash is present in both strokes. The green line represents the angle of attack programmed into the robot (α_{geom}); the red and blue lines represent the measured α_{aero} from the first and fourth strokes, respectively. The inset shows how each angle of attack is measured. (D) Comparison among measured net force (solid blue line), predictions of a quasi-steady translational model (green line) and predictions of a quasi-steady translational model corrected using the time courses of velocity and α_{aero} shown as blue traces in B and C (broken blue line). Traces show the mean values of a fourth down- and upstroke for both measured and predicted values. The corrected quasi-steady model correctly predicts a drop in force due to downwash ($\hat{t}=0.08$–0.18) but not an early increase due to wake capture ($\hat{t}=0$–0.08).

during wake capture (Fig. 11D). This suggests that the additional forces created as the wing passes through the wake of the previous stroke result from spatial and temporal changes in flow that are not accounted for in a quasi-steady model of a circulatory force. By contrast, the corrected quasi-steady model does predict with reasonable accuracy the later drop in force due to downwash.

Discussion

Using a dynamically scaled mechanical model of a flapping insect wing, we have quantified both the changes in fluid flow throughout a complete stroke and the influence of shed vortices from one stroke on the forces generated during the next. When a wing starts from rest, a leading edge vortex (LEV) develops gradually over the first 30% of the stroke while, simultaneously, a translational starting vortex (TSV) forms from the roll up of a sheet of vorticity under the wing. During this early growth phase, the wing generates a distinct force transient, previously attributed to added-mass acceleration. As the LEV attains a stable size, forces decay to a constant level (Fig. 4). Wing rotation prior to stroke reversal generates additional circulation and an increase in the strength of the LEV with a corresponding augmentation of force. Following reversal, the wing intercepts the shed vorticity from both the translation and rotation of the prior stroke, which modifies force production relative to the same phase of a stroke starting from rest (Fig. 5). Shed vorticity from prior strokes influences force production in two phases (Fig. 3). Forces early in the stroke are elevated due to a beneficial effect of the wake, while later in the stroke the downwash reduces the force generated by the wing. Understanding the physical basis for these effects

stroke (Fig. 11B), the aerodynamic angle of attack, α_{aero}, estimated from the mean orientation of flow within the rectangular region was between 10° and 20°. Substituting these values into the quasi-steady model of translational force (Sane and Dickinson, 2002) explains less than 65% of the peak force

in this simplified pattern of wing motion should provide insight for more complicated kinematic patterns across insect diversity and help to construct a general model of animal flight.

Quasi-steady models and the first moment of vorticity

Forces generated once the LEV has reached a stable size are well-approximated by a quasi-steady semi-empirical model (Sane and Dickinson, 2002). This is of course expected, because this model uses an empirical force coefficient that is itself measured under conditions of constant velocity. When a stable distribution of vorticity is attached to the wing, changes in the first moment of vorticity (γ; equation 1) result from the motion of the vorticity distribution through the fluid, conditions that satisfy the quasi-steady assumptions. This convergence was described by Wu (1981), who noted that one may derive the Kutta–Joukowski theorem from equation 1 for a wing moving at constant velocity with bound circulation.

Consistent with other experimental studies of impulsively started plates and bluff bodies (Hamdani and Sun, 2000; Odar and Hamilton, 1964; Sarpkaya, 1982, 1991, 1992), we measured a large force transient at the onset of motion. Although this transient has been previously attributed to added mass (Sane and Dickinson, 2002), quasi-steady approximations do not accurately capture the precise time course of this early force peak. The results of DPIV show that this early force occurs before the LEV attains its final size (Fig. 4) and thus cannot be explained by a steady-state circulation. However, the time course of force at the start of translation matches well with the time derivative of γ (Fig. 8). This confirms the computational work of Hamdani and Sun (2000), who used CFD to simulate the forces created by an impulsively started flat-plate in two dimensions. The forces in their simulated flows, calculated according to equation 1, accurately predicted those measured in a prior experimental study (Dickinson and Götz, 1993). Together with this previous work, our results suggest that the time course of force production by an impulsively started wing may be roughly divided into two parts: an early phase in which the LEV grows rapidly followed by a subsequent period in which a stable LEV remains attached as the wing moves away from the starting vortex. During the first phase, γ increases largely due to the growth of vorticity, whereas later it rises more slowly due to the increasing separation between the LEV and the TSV. These two phases are directly observed as a change in the slope of γ in the two-dimensional simulations of Hamdani and Sun (2000).

The physical basis of the wake capture

A corrected quasi-steady model that accounts for the altered flow field caused by the shed vorticity of prior strokes cannot account for the elevated forces generated during wake capture (Fig. 11D). This result is consistent with the observation that the LEV is quite small at the time when the wake capture effect is greatest (Fig. 5). This condition is similar to that which occurs during the early transient following an impulsive start, in that the instantaneous magnitude of vorticity cannot account

for the forces generated by the wing. Thus, wake capture is a truly unsteady effect, and, in order to derive forces from the flow, it is necessary to employ a model, such as equation 1, that accounts for time-dependent changes in the flow. An inspection of vorticity fields indicates that their structure changes both in space and time at the start of the stroke. Unfortunately, attempts to calculate the first moment of vorticity proved unreliable in the current data set due to the flux across the boundaries of the visualized region. Thus, we could not confirm whether the derivative of γ measured within a span-wise section was consistent with the time course of forces during wake capture. However, given that the wing must move through a complex system of several shed vortices (Figs 5, 9, 10), the influence on the first moment of vorticity will be quite large. A thorough quantitative analysis will require a larger map of the flow around the wing that encloses all the salient features of the flow. Future studies must also take into account the three-dimensional nature of the flow.

The influence of downwash

Unlike the case of wake capture, our results suggest that quasi-steady models can account for the wake-dependent drop in force at midstroke (Fig. 3). This result is not surprising, given that the structure of the flow within the wake at this time consists of a relatively constant unidirectional downward flow below the wing. Thus, the flow pattern fulfills the basic assumptions for a classic induced drag model, in which downwash lowers the angle of aerodynamic angle of attack, thereby altering the steady-state circulation created by a wing or propeller. However, the present condition differs from induced drag in two important ways. First, the downwash effect is pulsatile; the downward flow generated by the shed vortices grows over the first half of the stroke but then slowly decreases (Fig. 10). This time dependence of the downwash explains why the force traces for the first and fourth strokes converge by $\hat{t}$=0.30. Second, in standard models of downwash (McCormick, 1995), the decrease in α_{aero} causes an increase in drag but no change in lift. However, this simplification is only valid for small angle approximations and unseparated flow – conditions that do no apply in the current case. For a flat wing moving at a large angle of attack, the effect of downwash will be a decrease in both lift and drag (Birch and Dickinson, 2001), which, except for the small drag component due to skin friction, are simply orthogonal components of a single pressure force that operates perpendicular to the surface of the wing (Dickinson, 1996; Usherwood and Ellington, 2002).

Comparison of experimental results with CFD simulations

Sun and Tang (2002) and Ramamurti and Sandberg (2002) have recently presented CFD models based on wing kinematics nearly identical to those used in this study, providing an opportunity to compare experimentally measured forces and flows with state-of-the-art computational techniques. The present study corroborates many aspects of these simulations. First, mean forces generated in the CFD models are within 15%

of those generated here [mean lift coefficient for a down/upstroke sequence: 1.2 (Sun and Tang, 2002); 1.29 (Ramamurti and Sandberg, 2002); 1.4 (present study)]. The source of this slight discrepancy is difficult to identify and might be due to variations in the precise kinematic patterns and wing morphologies used, computational inaccuracies or experimental error. Second, the general shape of the force traces in the simulations resembles the measured forces, particularly the translation phase during the middle of the stroke and the rotational lift phase at the end of each stroke. Sun and Tang (2002) attribute the increased lift and drag at the end of each stroke to the instantaneous increase in translational forces due to the 'pitching-up rotation' of the wing, a hypothesis that they claim contradicts that of Dickinson et al. (1999). It is not clear whether their 'pitching-up hypothesis' implies that rotational forces are caused by the increased angle of attack, which could thus be explained by a quasi-steady model, or a circulatory force due to the time-derivative of the angle of attack. If the former, this hypothesis is not consistent with experimental data (Dickinson et al., 1999; Sane and Dickinson, 2001, 2002). Collectively, these experiments show that wing rotation causes an augmentation of force that is not explained by a quasi-steady translation model that takes into account the instantaneous angle of attack. If, however, the hypothesis of Sun and Tang is that rotational forces are dependent on the angular velocity of the wing about its long axis ($d\alpha/dt$), then their view is entirely consistent with experimental data. Forces during rotation are proportional to $d\alpha/dt$ and vary linearly with the cord-wise position of the rotational axis (Dickinson, et al., 1999; Sane and Dickinson, 2002), in close agreement with theoretical predictions (Fung, 1969).

Thus, the only significant discrepancy between the simulated and empirical results is the prediction of an early force peak in the first and subsequent strokes. Sun and Tang (2002) claim to find no evidence of this wake capture peak, whereas the CFD simulations of Ramamurti and Sandberg (2002) show a wake capture peak that is consistent with prior experimental studies (Dickinson et al., 1999). Sun and Tang suggest that the force peak following stroke reversal is due to the rapid acceleration of the wing rather than the recapture of vorticity from the wake. However, this hypothesis was tested in the current study by directly comparing forces and flows in the presence and absence of prior strokes (Figs 3, 10). Although an impulsively started wing generates an acceleration-dependent force, the forces created by identical kinematics in the presence of a wake are unequivocally higher.

General significance for insect flight

Together with other recent experimental studies (Ellington et al., 1996; Dickinson et al., 1999; Sane and Dickinson, 2001, 2002; Srygley and Thomas, 2002), these results help to solidify an emerging picture of the force and flow dynamics of flapping wings. This study presents force measurements and flow patterns for an arbitrary pattern of wing motion, chosen in part because it creates forces by all the mechanisms currently known to function on single wings. For this reason, it represents a convenient model system for analyzing the underlying fluid mechanics of insect flight. This simple set of kinematics and the resulting time history of forces and flows should not be misinterpreted, however, as being characteristic of insects in general. The actual patterns of wing motion used by different insects, or any individual at different moments, are diverse (Srygley and Thomas, 2002). It remains to be determined how the relative importance of different mechanisms or the interactions among them change with evolution and behavior.

References

Bennett, L. (1970). Insect flight: lift and the rate of change of incidence. *Science* **167**, 177-179.

Birch, J. M. and Dickinson, M. H. (2001). Spanwise flow and the attachment of the leading-edge vortex on insect wings. *Nature* **412**, 729-733.

Brodsky, A. K. (1994). *The Evolution of Insect Flight*. Oxford: Oxford University Press.

Cloupeau, M., Devillers, J. F. and Devezeaux, D. (1979). Direct measurements of instantaneous lift in desert locust; comparison with Jensen's experiments on detached wings. *J. Exp. Biol.* **80**, 1-15.

Daniel, T. L. (1984). Unsteady aspects of aquatic locomotion. *Am. Zool.* **24**, 121-134.

Denny, M. W. (1988). *Biology and the Mechanics of the Wave-Swept Environment*. Princeton: Princeton University Press.

Denny, M. W. (1993). *Air and Water. The Biology and Physics of Life's Media*. Princeton: Princeton University Press.

Dickinson, M. H. (1994). The effects of wing rotation on unsteady aerodynamic performance at low Reynolds numbers. *J. Exp. Biol.* **192**, 179-206.

Dickinson, M. H. (1996). Unsteady mechanisms of force generation in aquatic and aerial locomotion. *Am. Zool.* **36**, 537-554.

Dickinson, M. H. and Götz, K. G. (1993). Unsteady aerodynamic performance on model wings at low Reynolds numbers. *J. Exp. Biol.* **174**, 45-64.

Dickinson, M. H. and Götz, K. G. (1996). The wake dynamics and flight forces of the fruit fly *Drosophila melanogaster*. *J. Exp. Biol.* **199**, 2085-2104.

Dickinson, M. H., Lehmann, F. O. and Sane, S. (1999). Wing rotation and the aerodynamic basis of insect flight. *Science* **284**, 1954-1960.

Ellington, C. P. (1984). The aerodynamics of hovering insect flight. V. A vortex theory. *Phil. Trans. R. Soc. Lond. B* **305**, 115-144.

Ellington, C. P., Van Den Berg, C., Willmott, A. P. and Thomas, A. L. R. (1996). Leading-edge vortices in insect flight. *Nature* **384**, 626-630.

Fung, Y. C. (1969). *An Introduction to the Theory of Aeroelasticity*. New York: Dover.

Grodnitsky, D. L. and Morozov, P. P. (1993). Vortex formation during tethered flight of functionally and morphologically two-winged insects, including evolutionary considerations on insect flight. *J. Exp. Biol.* **182**, 11-40.

Hamdani, H. and Sun, M. (2000). Aerodynamic forces and flow structures of an airfoil in some unsteady motions at small Reynolds number. *Acta Mech.* **145**, 173-187.

Liu, H., Ellington, C. P., Kawachi, K., Van Den Berg, C. and Willmott, A. (1998). A computational fluid dynamic study of hawkmoth hovering. *J. Exp. Biol.* **201**, 461-477.

Liu, H., Wassersug, R. J. and Kawachi, K. (1996). A computational fluid dynamics study of tadpole swimming. *J. Exp. Biol.* **199**, 1245-1260.

McCormick, B. W. (1995). *Aerodynamics, Aeronautics, and Flight Mechanics*. Second edition. New York: John Wiley & Sons.

Noca, F., Shiels, D. and Jeon, D. (1997). Measuring instantaneous fluid dynamic forces on bodies, using only velocity fields and their derivatives. *J. Fluids Struct.* **11**, 345-350.

Noca, F., Shiels, D. and Jeon, D. (1999). A comparison of methods for evaluating time-dependent fluid dynamic forces on bodies, using only velocity fields and their derivatives. *J. Fluids Struct.* **13**, 551-578.

Odar, F. and Hamilton, W. S. (1964). Forces on a sphere accelerating in a viscous fluid. *J. Fluid Mech.* **18**, 302-314.

Raffel, M., Willert, C. and Kompenhans, J. (1998). *Particle Image Velocimetry: a Practical Guide*. Berlin: Springer-Verlag.

Ramamurti, R. and Sandberg, W. C. (2002). A three-dimensional computational study of the aerodynamic mechanisms of insect flight. *J. Exp. Biol.* **205**, 1507-1518.

Rayner, J. M. V. (1979). A new approach to animal flight mechanics. *J. Exp. Biol.* **80**, 17-54.

Sane, S. P. and Dickinson, M. H. (2001). The control of flight force by a flapping wing: lift and drag production. *J. Exp. Biol.* **204**, 2607-2626.

Sane, S. P. and Dickinson, M. H. (2002). The aerodynamic effects of wing rotation and a revised quasi-steady model of flapping flight. *J. Exp. Biol.* **205**, 1087-1096.

Sarpkaya, T. (1982). Impulsively-started flow about four types of bluff body. *J. Fluids Eng.* **104**, 207-213.

Sarpkaya, T. (1991). Nonimpulsively started steady flow about a circular cylinder. *AIAA J.* **29**, 1283-1289.

Sarpkaya, T. (1992). Brief reviews of some time dependent flows. *J. Fluids Eng.* **114**, 283-298.

Sarpkaya, T. (1996). Unsteady flows. In *Handbook of Fluid Dynamics and Fluid Machinery*, vol. 1 (ed. J. A. Schetz and A. E. Fuhs), pp. 697-732. New York: John Wiley & Sons.

Spedding, G. R., Rayner, J. M. V. and Pennycuick, C. J. (1984). Momentum and energy in the wake of a pigeon (*Columba livia*) in slow flight. *J. Exp. Biol.* **111**, 81-102.

Srygley, R. B. and Thomas, A. L. R. (2002). Unconventional lift-generating mechanisms in free-flying butterflies. *Nature* **420**, 660-664.

Sun, M. and Tang, J. (2002). Unsteady aerodynamic force generation by a model fruit fly wing in flapping motion. *J. Exp. Biol.* **205**, 55-70.

Usherwood, J. R. and Ellington, C. P. (2002). The aerodynamics of revolving wings I. Model hawkmoth wings. *J. Exp. Biol.* **205**, 1547-1564.

Wilkin, P. J. and Williams, M. H. (1993). Comparison of the aerodynamic forces on a flying sphingid moth with those predicted by quasi-steady theory. *Phys. Zool.* **66**, 1015-1044.

Willmott, A. P., Ellington, C. P. and Thomas, A. L. R. (1997). Flow visualization and unsteady aerodynamics in the flight of the hawkmoth *Manduca sexta*. *Phil. Trans. R. Soc. Lond.* **352**, 303-316.

Wu, J. C. (1981). Theory for aerodynamic force and moment in viscous flows. *AIAA J.* **19**, 432-441.

Zanker, J. M. and Götz, K. G. (1990). The wing beat of *Drosophila melanogaster*. II. Dynamics. *Phil. Trans. R. Soc. Lond. B* **327**, 19-44.